Quasi-isotropic Surface Plasmon Polariton Generation through Near-Field Coupling to a Penrose Pattern of Silver Nanoparticles

Ruggero Verre,[†,*] Tomasz J. Antosiewicz,[†,‡] Mikael Svedendahl,[†] Kristof Lodewijks,[†] Timur Shegai,[†] and Mikael Käll[†,*]

[†]Department of Applied Physics, Chalmers University of Technology, 412 96 Göteborg, Sweden, and [‡]Centre of New Technologies, University of Warsaw, Banacha 2c, 02-097 Warsaw, Poland

ABSTRACT Quasicrystals are structures that possess long-range order without being periodic. We investigate the unique characteristics of a photonic quasicrystal that consists of plasmonic Ag nanodisks arranged in a Penrose pattern. The quasicrystal scatters light in a complex but spectacular diffraction pattern that can be directly imaged in the back focal plane of an optical microscope, allowing us to assess the excitation efficiency of the various diffraction modes. Furthermore, surface plasmon polaritons can be launched almost isotropically through near-field grating coupling when the quasicrystal is positioned close to a homogeneous silver surface. We characterize the dispersion relation of the different excited plasmon modes by reflection measurements and simulations. It is demonstrated that the quasicrystal in-coupling efficiency is strongly enhanced compared to a nanoparticle array with the same particle density but only short-range lateral order. We envision that the system can be useful for a number of advanced light harvesting and optoelectronic applications.

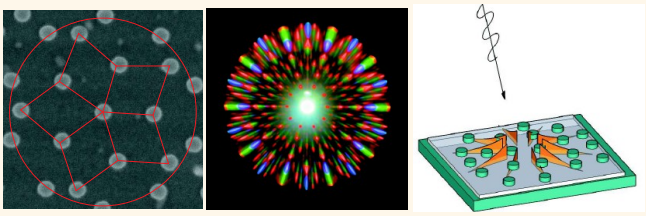

KEYWORDS: quasicrystal · plasmonic nanoantenna · diffraction grating · surface plasmon polariton · Fourier plane · light management

The distinctive features of regular crystals arise from their symmetry properties, as described by the 14 different Bravais lattices in three dimensions. The translational symmetry of regular crystals allows for the application of Bloch's theorem, which implies that the eigenstates of the system can be described through energy bands in reciprocal space.[1] Quasicrystals, on the other hand, are a class of materials that possess long-range order but lack translational symmetry.[2,3] A quasicrystal can be constructed by using the projection theorem,[4] in which case the quasiperiodic structure is the result of the projection from a higher dimensional regular lattice into a lower dimension. The result of this procedure is a structure with a well-defined diffraction pattern that densely fills reciprocal space but with point symmetries that are impossible in ordinary periodic structures. In a sense, quasicrystals can be thought of as intermediate between amorphous solids and regular crystals. Although Bloch's theorem cannot be strictly applied to a quasicrystal, it is still possible to identify pseudo-Brillouin zones and complex collective band structure effects.[5]

From the point of view of optics, quasicrystal structures have recently been investigated in the context of a number of photonic applications, like broadband lasing,[6] negative refraction,[7] waveguiding,[8] light-emitting devices,[9] and enhanced optical transport.[10−12] The proposed advantages of photonic quasicrystals, compared to standard photonic crystals, typically rely on the presence of multiple band gaps[13] and/or a more isotropic behavior, which results from the large number of reciprocal lattice vectors present in the first pseudo-Brillouin zone.[14]

Over the past few years, several research groups have investigated quasicrystal structures in conjunction with various surface plasmon resonance phenomena in metal

* Address correspondence to ruggero.verre@chalmers.se; mikael.kall@chalmers.se.

Received for review June 12, 2014 and accepted September 2, 2014.

Published online September 02, 2014
10.1021/nn503195n

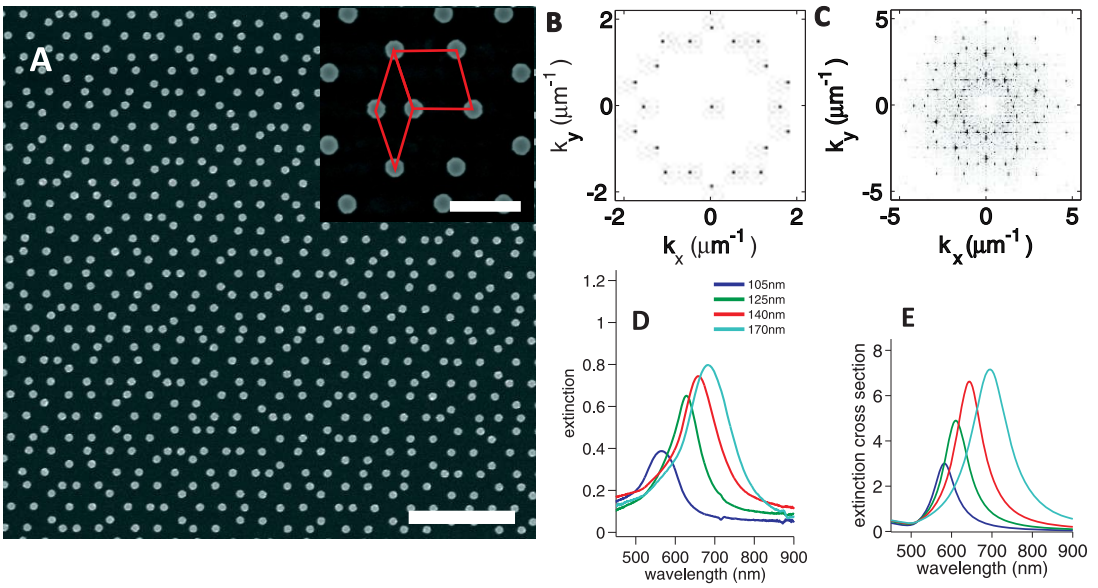

Figure 1. (A) SEM image of a plasmonic Ag particle quasicrystal. The scale bars are 2 μm and 500 nm for the large image and the inset, respectively. The 2D Fourier images with (B) high and (C) low contrast reveal the 10-fold symmetry of the Penrose pattern and numerous higher order diffraction modes characteristic for quasiperiodic structures. (D) Extinction measurements for PQs with different NP diameter and (E) the simulated extinction cross section for a Ag ellipsoid embedded in a dielectric environment with a refractive index of 1.15.

nanostructures. Several types of two-dimensional (2D) plasmonic quasicrystals (PQs) and aperiodic structures have been produced, and their optical properties investigated.[15−22] PQs have been used for extraordinary light transmission,[23−26] subdiffraction focusing,[27,28] solar light harvesting,[29−31] refractometric sensing,[32,33] and surface-enhanced Raman scattering.[34] The possibility of using macroscopic 2D PQs for applications has recently been highlighted by the development of Moire lithography[35,36] and other methods[37] that allow for patterning of large areas rapidly and at low cost.

In this article, we investigate the properties of a PQ diffraction grating based on silver nanodisks made by electron beam lithography. We analyze the diffraction pattern resulting from the distribution of reciprocal lattice vectors characterizing the quasiperiodic pattern using Fourier imaging and optical spectroscopy, and we determine the diffraction efficiency of each mode directly. The PQ is then used as an in-coupling device for surface plasmon polaritons (SPPs) propagating on a silver surface placed underneath. This system supports several excitation modes, and its dispersion is calculated and compared to the experiment.

RESULTS AND DISCUSSION

The Penrose pattern was generated using the deflation rule,[38] and an approximant unit cell of $8 \times 10\ \mu m^2$ was repeated to obtain larger structures. The pattern consists of Ag nanodisks with 40 nm height and diameter varying from 100 to 170 nm (see Methods). The distance between different nanoparticles (NPs), as defined by the side length of the rhomboidal repetition unit typical of a Penrose pattern,[39] was chosen to be 420 nm. The resulting structure, imaged using a scanning electron microscope (SEM), is shown in Figure 1A. The 2D Fourier transform (FT) of the image reveals the 10-fold symmetry typical of the Penrose pattern (see Figure 1B).

When the contrast in the Fourier image is decreased, additional peaks appear. These peaks correspond to higher order modes that densely fill the reciprocal space of any quasiperiodic pattern.[2,12] We performed a systematic characterization of the optical transmittance properties of the PQ structures by measuring extinction spectra using unpolarized light incident normal to the sample surface. As expected from the relatively large distance between the particles, which prevents near-field coupling, we found that the structures support one dominant plasmon excitation mode, depicted in Figure 1D, namely, the in-plane dipolar localized surface plasmon resonance (LSPR) of an individual Ag disk. The LSPR peak red-shifts for increasing NP diameter, a trend that can be reproduced by simulating the system as an isolated elliptical NP with the same dimensions as in the experiment but surrounded by a uniform medium with an effective refractive index of 1.15 (see Figure 1E).

The PQs thus behave similarly to a collection of noninteracting plasmonic nanoparticles in extinction measurements (Figure 1D);[40] that is, they exhibit only a single dipolar LSPR, and there are no spectral features indicating either near-field optical interactions between the particles[41,42] or diffractive far-field coupling effects.[43] As can be seen in Figure 2, however, the PQs

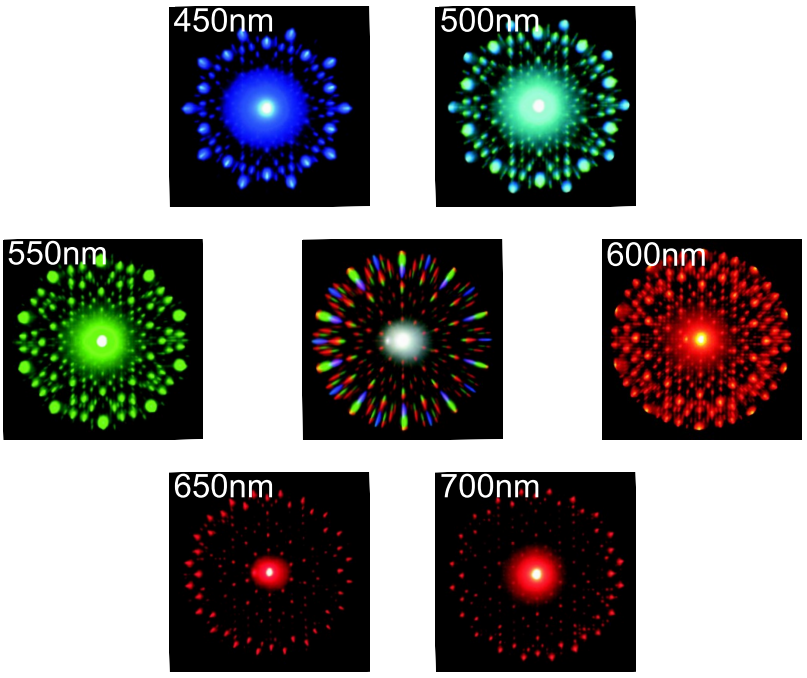

Figure 2. Optical Fourier images of a Ag PQ. A panchromatic (center) and several quasi-monochromatic (40 nm wide band-pass) images are shown. The optical Fourier image mirrors the 2D FFT of the SEM image. For increasing wavelengths the diffraction orders move further away from the central zeroth order. Inside the circle formed by the first-order spots (brightest points for $\lambda \leq 550$ nm) higher order diffraction modes are visible.

exhibit striking diffraction patterns when illuminated with collimated light. The scattered light is here directly monitored in an optical microscope by imaging the objective's back focal plane (Fourier plane). Each point thus corresponds to a particular diffraction angle, and the image represents the collective behavior of all particles within the objective's field of view.[44]

It is evident that the panchromatic and quasi-monochromatic images in Figure 2 exhibit 10-fold symmetry and show a pattern similar to the FT calculated from the SEM image presented in Figure 1. As the optical Fourier images turned out to be essentially independent of the NP diameter, we will from now on focus on NPs having 140 nm diameter. Each smeared-out rainbow spot in the central image of Figure 2 corresponds to one or more overlapping diffraction orders. By inserting 40 nm band-pass filters in front of the light source, the Fourier pattern image can be spectrally resolved and more easily analyzed. We first notice that the diffraction spots clearly move toward the edge of the collection zone in the Fourier plane, corresponding to higher diffraction angles, for increasing wavelength, as expected. The diffraction condition is met whenever the in-plane wavevector component of a diffracted beam $\mathbf{k}_{o,||}$ is equal to the sum of the wavevectors carried by the incident light $\mathbf{k}_{i,||}$ and $\mathbf{G}$ generated by the diffraction grating:

$$\mathbf{k}_{o,||} = \mathbf{k}_{i,||} + \mathbf{G} \tag{1}$$

In the case of a quasicrystalline structure, where multiple modes are excited at the same time,

$$\mathbf{G} = \frac{2\pi}{a}\mathbf{k} \tag{2}$$

where $\mathbf{k} = \sum_{j=1}^{5} c_j \mathbf{k}_j$ is any linear combination of the five base vectors $\mathbf{k}_j$ (given by $e^{i\pi/5}$) required to describe the 10-fold symmetric Penrose pattern. The integers c_j define a particular reciprocal vector $c = [c_1, c_2, c_3, c_4, c_5]$, a is the periodicity corresponding to the first pseudo-Brillouin zone, and the scattering order is defined as $n = \sum_{j=1}^{5} |c_j|$.[36] Since the wavenumber of light is given by $k_o = 2\pi\lambda^{-1}$ and the in-plane component is given by eq 1, then the out-of-plane component for shorter wavelengths increases and the outgoing wavevector $\mathbf{k}_o$ is directed at angles closer to the surface normal for a certain diffraction component.

In the following, each diffraction spot in the Fourier image in Figure 2 will be assigned to a specific mode and its excitation efficiency will be extracted. This is done by first reconstructing the full reciprocal space for a 10-fold symmetric PQ by analyzing the SEM FT. The first order is then identified by using five reciprocal vectors and their opposite, each shifted by $e^{i\pi/5}$. The second order is then given by the sum of any two of these vectors (including multiples of the same), the third by the sum of any three of them, and so on. The results for the reciprocal vectors close to the origin are shown in Figure 3. One immediately notices close similarities between the 40 nm band-pass Fourier spectrum collected for 1 s at 500 nm and the reciprocal

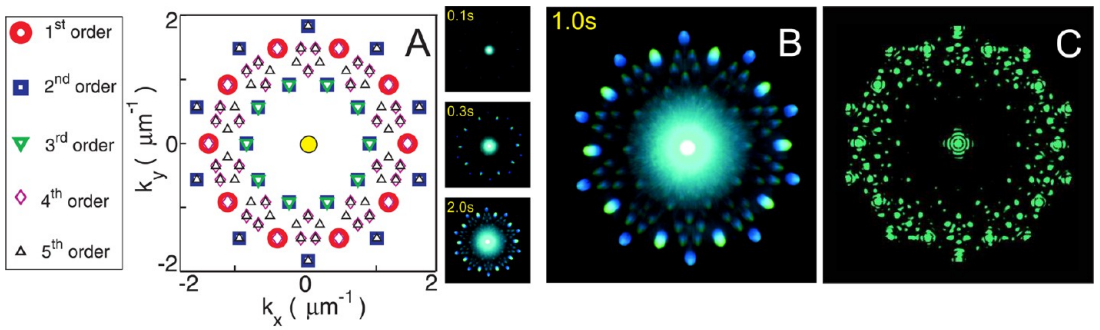

	1st	2nd/3rd	2nd/5th	4th/5th outer	4th/5th inner	5th
2D-FT	1	0.18	1.08	0.24	0.13	0.2
Exp	1	0.17	0.4	0.16	0.13	0.14
Theory	1	0.03	0.43	0.1	0.06	0.04

Figure 3. (A) Reconstructed distribution of reciprocal vectors for the PQ with relative mode assignment. (B) Optical Fourier images of a PQ collected at 500 nm for different exposure times. In particular, modes up to the fifth can be seen. (C) Reconstructed scattered field at 500 nm using eq 3 (see text for details). In the table we enumerate the intensities of the different peaks in the 2D FT SEM image, in the measured optical Fourier, and of the simulated scattered fields. The different modes are assessed following the nomenclature in A, and they are normalized by the first-order peak intensity.

image. What is lacking in the reciprocal image is the excitation efficiency of the different modes. However, this information is contained within the intensity of the peaks in the optical Fourier image. Hence, Fourier imaging allows one to *directly extract* the relative efficiency of each diffraction mode by analyzing the peak intensity for different exposure times. This is shown in the table of Figure 3, where different peak intensities have been measured for the different diffracted spots. After the first-order mode, the most intense peak is assigned to a second-order mode overlapped with a fifth-order mode. Other modes are also recognized and attributed to a combination of second and third order, fourth and fifth, and a purely fifth-order mode, each having similar efficiency. It is interesting to note that magnitudes of the various peaks of the 2D FT of the SEM do not exactly reproduce the ones calculated from the optical Fourier images (see table, first row). This is particularly obvious for the second/fifth-order mode, whose amplitude is even greater than the one measured in the experiment. The reason is a complex interference between the scattered fields of the different particles. As the real-space structure may be expressed as a convolution of one disk and the array factor, its Fourier transform is the product of the isolated disk form factor *F* and the structure factor of the quasicrystal arrangement *S*. The intensity at a given angle in the far field can be expressed as[45,46]

$$I(\theta,\phi) = F(\theta,\phi)\,S(\theta,\phi) = F(\theta,\phi)\sum_{i,j}(e^{i\mathbf{q}\cdot\mathbf{r}_i})(e^{-i\mathbf{q}\cdot\mathbf{r}_j}) \quad (3)$$

In eq 3, **r** are the disk coordinates of the Penrose pattern and **q** is the wavevector connecting the nanoparticle centers to a given solid angle. In eq 3 the exponential arguments represent the phase lag of the electric field generated by the different particles. Such fields are allowed to interfere, generating the complex diffraction pattern of Figure 3. We use eq 3 for a more quantitative analysis of the results. The form factor was calculated as the scattered field of an isolated dipole at λ = 500 nm placed in air on top of a glass surface (n = 1.5).[47] The only free parameter was the distance between the dipole and the interface, which was assumed to be δ = 20 nm, that is, half of the nanoparticle height. The scattered field was calculated by summing the contribution over 600 particles, which produced a good convergence of the scattering pattern. The simulated relative peak intensities are presented in the table. It can be noticed that the agreement between the experiment and the simulation for the second/fifth mode is quite good, confirming that the form factor of the isolated particle plays a crucial role. The differences between experiment and theory from the other modes could arise from approximating the nanoparticle as a point dipole and by the fact that the measurements were performed with a 40 nm bandpass while simulations were performed at a single wavelength. Also, the exact experimental determination between the different peak intensities is complicated by the limited dynamic range of the image sensor (saturation) and the presence of a background due to diffuse scattering and stray light. In particular, this effect could be dramatic for the modes located close to the center of the Fourier plane due to a large background for the directly transmitted light, which is not taken into account in the simulations. Effectively, the mismatch between experiment and theory increases for the modes closer to the center of the Fourier plane.

Now that we have analyzed the fascinating far-field optical properties of nanoparticle PQs, we will use the same structure for coupling light into propagating

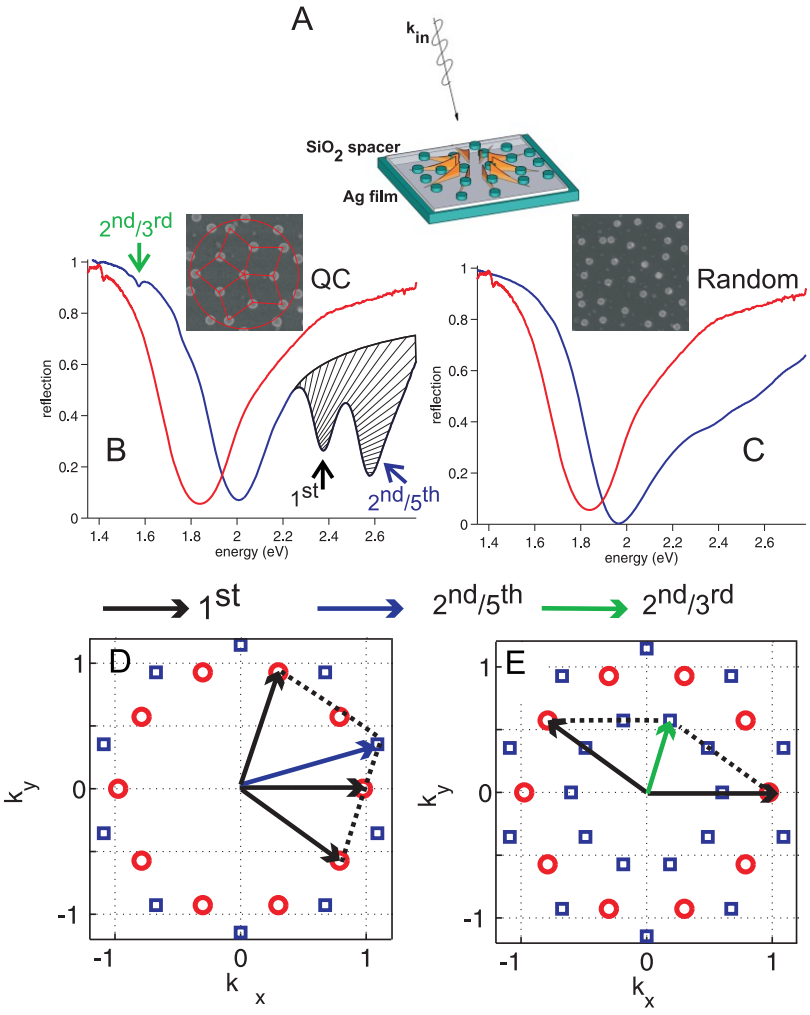

Figure 4. (A) Schematic configuration to launch SPP from a PQ grating on top of a Ag mirror and a 60 nm SiO_2 dielectric spacer. Normal incidence reflection measurements for a PQ and a random NP distribution are plotted by the violet lines in B and C, respectively. The red line corresponds to the calculated $(1 - e_{QC})^2$ where e_{QC} is the extinction as measured in Figure 1D for a PQ having the same diameter (140 nm) but placed on a glass slide. Multiple reflection dips can be seen in the case of the PQ in-coupled to the Ag mirror, and they correspond to different Bragg modes of the plasmonic grating. The SPP in-coupling efficiency is estimated by analyzing the shaded area in B. The large dips at 2.35 and 2.6 eV are related to the first and second/fifth-order reciprocal vector schematically depicted in D, while the small dip observed at ~1.6 eV is related to a hybrid second/third-order mode represented in E. The explicit addition of first-order vectors in D and E clearly represents only the second-order modes.

plasmons using near-field coupling. To this end, we fabricated the PQ described above on a 60 nm SiO_2 dielectric spacer layer deposited on a Ag mirror formed by an optically thick (100 nm) silver film (see sketch in Figure 4A). The PQ now acts as a grating coupler for propagating SPPs on the interface between the SiO_2 spacer and the Ag surface. The fact that there is a strong near-field interaction between the nanodisk layer and the mirror can be concluded from inspection of reflection spectra measured at normal incidence (see Figure 4B, violet curve), in comparison to the reflection that would be generated if the PQ was placed at large distance from the mirror (red curve). In the latter case, the response of each substructure, *i.e.*, the mirror and the PQ, would simply be multiplicative, and the reflection can hence be calculated, in a first approximation, as $(1 - e_{PQ})^2$, where e_{PQ} is the extinction measured for the PQ supported on glass. We have assumed that the mirror has 100% reflectance while the specular reflectance of the PQ layer is negligible, which is a reasonable assumption considering the low particle coverage. While prominent LSPR minima are visible in both spectra at ~1.9 eV, additional dips at 2.35 and 2.6 eV are present only in the near-field coupled system (violet line). This proves that near-field interactions between the evanescent field characteristic to the LSPR generated on the Ag nanoparticles and the Ag film underneath are crucial for efficient coupling of light into the SPPs. However, the long-range order of the quasicrystal is also fundamental to achieve efficient and effective in-coupling. In Figure 4C it is shown that when the PQ is substituted by a randomly dispersed nanodisk distribution with similar particle density and same dimensions, the two prominent dips at high energy disappear and only the LSPR signature at 2.0 eV remains. Note that the difference in

LSPR positions between the bare PQ and the coupled system can be explained by the presence of the Ag film, which increases the effective refractive index around the nanoparticle, thus causing a red-shift. The slight mismatch in LSPR dip position between the random and quasicrystalline case is the result of different coupling conditions for PQ and amorphous arrays.[48] Also, the reflectance of randomly dispersed nanodisks at high energies is lower for nanodisks on top of the Ag mirror when it is compared to nanodisks on glass. In the former case, as the nanodisks are still in close proximity to the mirror, SPPs can still be launched on the surface. However, without the coherence the quasicrystalline arrangement provides, the effects are blurred and no clear minima can be identified.

We now turn to the complicated issue of mode assessment in the PQ-mirror system. A propagating SPP in the PQ case can be excited efficiently only when the sum of the in-plane wavevector component of the incident field and the grating vector **G** matches the SPP wavevector $\mathbf{k}_{SPP}$:

$$\mathbf{k}_{SPP} = \frac{\omega}{c}\sqrt{\frac{\varepsilon\varepsilon_m}{\varepsilon+\varepsilon_m}} = \mathbf{k}_{i,\parallel} \pm \mathbf{G} \qquad (4)$$

In eq 4, ω is the light angular frequency, c is the speed of light, ε is the tabulated Ag dielectric function,[49] and ε_m is the dielectric medium on top of the mirror. In the calculation we assume ε_m to be a homogeneous mixture of SiO_2 (60%) and air (40%). These values have been chosen to fit the energy of the first-order dip at 2.3 eV. By solving eq 4, the dip at 2.6 eV can then be assigned to excitation of the second most intense mode measured in the Fourier space, *i.e.*, the hybrid second/fifth-order mode outlined in Figure 4D. At the reflection minima, energy is coupled into the Ag film due to the combined effect of the long-range quasicrystalline order and the near-field coupling between the LSPR and the SPP. As measurements are performed at normal incidence, there are 10 wavevectors that satisfy eq 4. This occurs symmetrically around the origin of the first pseudo-Brillouin zone as depicted in Figure 4D. The behavior of the PQ is obviously more isotropic in comparison to what can be expected for a regular periodic crystal,[20] because light is simultaneously channeled into SPPs along 10 directions, while the maximum number of directions for a regular 2D crystal is 6. The dips in reflection due to SPP excitation for the two modes at 2.35 and 2.6 eV are around 0.35 and 0.53, respectively (as estimated by analyzing the shaded area in Figure 4B). Therefore, each of the 10 channels carries 3.5% and 5.3% of the incident light with respect to the input light intensity in free space. Light is thus routed nearly isotropically into different directions with high efficiency.

For a system of noninteracting particles, which is a good approximation in the present case, the overall far-field diffraction efficiency is simply given by the product of the single-particle scattering cross section and the particle surface density. While it is difficult to directly measure the scattering cross section for these samples using the traditional integrating sphere methodology, with the dipole model used to simulate the extinction data (Figure 1E), we estimate that 75% of the light is diffracted, while 25% is absorbed. This light is then divided into different channels according to the structure factor, but the total amount of scattered/diffracted light is the same independent of the particle arrangement, meaning that each diffraction order in a sample with high symmetry (like the Penrose pattern) carries less energy than a diffraction order in a periodic array (given that the overall particle density is the same). However, this argument is based only on far-field scattering/diffraction and is probably only approximately correct in the present case due to the near-field coupling mediated by long-range SPP modes.

Interestingly, a smaller dip is also observed around 1.6 eV for the PQ on top of the Ag film. This corresponds in the simulation to the excitation of the overlapping second- and third-order mode, and the small intensity is related to the low excitation efficiency of the mode (see table in Figure 3). It is interesting to note that, despite being a higher order mode, it is present at lower energy. This phenomenon can take place only for quasi-periodic structures, where the number of reciprocal base vectors surpasses the dimensionality of the system. In this case, in fact, it is possible to find suitable combinations of base vectors such that their sum will end up being smaller than the first-order mode vectors (see for example the sketch in Figure 4E).

In order to complete the understanding of the optical property of the system, the *full* dispersion relation for the structure was also measured by angle-dependent reflection spectroscopy (see Figure 5A). While the LSPR dip appears almost constant in intensity and energy, the other minima clearly split into multiple bands. This is additional confirmation that the modes observed at normal incidence are indeed related to multiple SPP modes generated by the PQ. The results are also compared with theory by solving eq 4 at each angle of incidence; for results see Figure 5B. The presence of the NP layer is neglected in the SPP dispersion calculation, which makes an exact indexing of each measured mode in the experiment complicated. Nevertheless, the calculated first- and second-order modes, shown in Figure 5B, match both modes located above the LSPR resonance as well as the weak mode around 1.6 eV

The measured data also clearly show anticrossing between the LSPR and the $[\bar{1}0000]$ mode and two degenerate $[0\bar{1}000]$/[00001] modes, as well as between the LSPR and two degenerate second-order $[0\bar{1}010]$/$[00\bar{1}01]$ modes. For these reasons and due to the numerous modes present in the system (see Figure S3 for a full indexing up to the third-order mode), in some

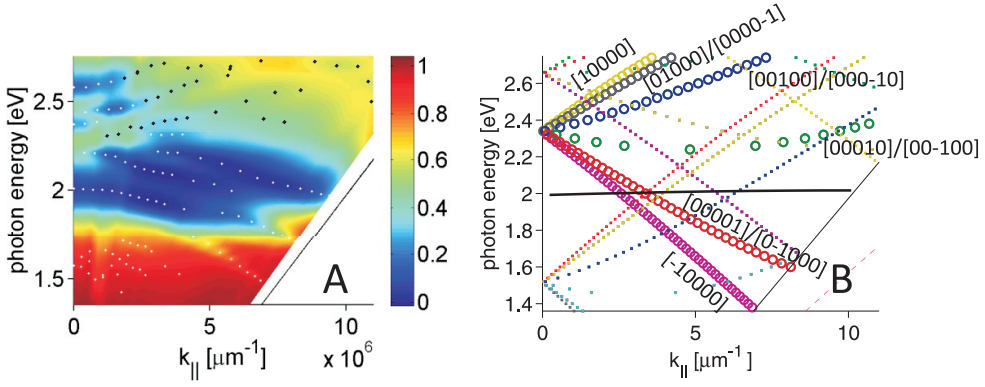

Figure 5. (A) Reflection spectra *versus* incidence angle, expressed as in-plane wavevector. The splitting of the different modes can be clearly observed. The dots (white and black) correspond to clear reflection minima. (B) Simulation of the diffraction modes for a PQ distributed in a Penrose pattern and calculated using eq 4. The large symbols represent the first-order modes, while the remaining ones refer to second-order modes. The horizontal line at 2 eV indicates the LSPR reflection dip.

cases mode identification is not straightforward. Finally, the dispersion relation depends on the polarization of the incident light and on the azimuthal orientation of the sample (see Supporting Information Figure S1 and Figure S2). While the former is due to different LSPR excitation efficiencies and in-coupling efficiencies between the LSPR and the SPPs, the latter is related to the symmetry of the system with respect to the plane of incidence. For the case shown in Figure 5B of the 10 possible first-order modes 8 are degenerate, but when the plane of incidence is rotated by $\pi/10$, the degeneracy would include all these modes. Therefore, we limit ourselves to studying the semiquantitative agreement between measured and calculated modes instead of doing a full indexing of all possible modes in this complex system.

The realized QC system enables launching of SPP on the Ag mirror placed underneath with high efficiency and isotropy. A similar configuration was recently exploited to analyze the interaction between SPPs and LSPRs in a periodic plasmonic metasurface,[50] but we here demonstrate the importance of the in-coupling mechanism, and we are able to excite multiple modes using larger point symmetries. While it is true that an SPP could also be launched by directly patterning the Ag film, in the present configuration the plasmonic disks are separated 60 nm from the film, and they perturb the SPP only slightly. The SPPs are expected then to propagate a longer distance, and the light carried can be used for real optoelectronic devices and advanced light management. For example, energy can be launched along multiple directions and imaged by patterning diffraction grooves on the Ag film. In this way, 10 parallel light channels can in principle be obtained at the same time and sensed or utilized. Other approaches were proposed to realize light directionality,[51] and many structures working at visible frequencies were yet produced using plasmonic objects.[52−54] However, previous reports concentrated either on modifying the far-field radiation patterns[55] or on realizing an efficient near-field coupling between a plasmonic antenna and an emitter.[56−58] In the present case, the proposed plasmonic router device acts mainly as an optical element, which could allow for further parallel manipulations of the different SPP channels, and this could be realized in a planar device fabricated with standard lithographic processes. We envision that the system could also be used as a refractive index based biosensor. In this case, shifts in each peak position upon changes in the refractive index surrounding the NP layer can be monitored for multiple peaks,[32] and particularly high sensitivity for certain modes upon different illumination conditions could be achieved.

CONCLUSIONS

We analyzed the response of a plasmonic quasicrystal arranged in a Penrose pattern. The structure acts as a diffraction grating, with multiple components excited under collimated illumination. We developed a method to directly extract the efficiency of each mode by imaging the optical Fourier plane of the PQ and launched SPP on a Ag film placed underneath. The system hence acts as an in-coupling device, with light channeled into various directions in an almost isotropic fashion. This effect takes place at multiple wavelengths with high efficiency. The system could then be used for optoelectronic devices.

EXPERIMENTAL METHODS

Sample Fabrication. Plasmonic quasicrystals were produced using a JEOL 9300X electron beam lithography system. PMMA A2 was spun on various substrates, and the surface exposed to different electron beam doses to obtain nanoparticles having different diameters. After development, the samples were

exposed to metal evaporation and lift-off. A 2 nm Ti layer was deposited prior to Ag evaporation to ensure proper adhesion on the substrate. Prior to measurements, the samples were annealed at 250 °C for 10 min in an Ar atmosphere to improve the metal crystallinity. In order to investigate the coupling between the plasmonic grating and a homogeneous surface made of the same material, an optically thick (100 nm) silver film and a 60 nm SiO_2 spacer were evaporated before the lithographic step.

Optical Characterization. Transmission measurements were performed using an inverted Nikon microscope. Light was focused using a 20× air objective with NA = 0.5, and the transmitted light captured using a Nikon 10× air objective, NA = 0.3. The signal was collected by an Andor spectrometer equipped with an iDus camera. For Fourier imaging, particular wavelengths were selected using a 40 nm band-pass filter placed directly after the light source, and a collimated beam was used to illuminate the sample. The diffracted light was then imaged in the Fourier plane using a Nikon 60× TIRF objective, NA = 1.49, and a Nikon camera. To extract the peak efficiencies from the Fourier images, the recorded image was first converted in a high-resolution black and white image, and the peak intensity was then measured in the brightest points.

Reflection measurements were performed using a homemade setup, consisting of a halogen light source, a variable-angle goniometer, and a fiber-coupled B&W Tek spectrometer (BRC711E). Measurements between 1.4 and 2.8 eV (450 to 900 nm) were performed. The same type of Ag mirror utilized in the in-coupling device was also used as a reference for the reflection measurements.

Conflict of Interest: The authors declare no competing financial interest.

Supporting Information Available: Reflection measurements for the plasmonic coupling device for different azimuthal orientations and dispersion relations for different polarization states. Simulated dispersion relations for the first three order modes, with full indexing. This material is available free of charge *via* the Internet at http://pubs.acs.org.

Acknowledgment. This work was supported by the Knut and Alice Wallenberg Foundation, the Swedish Research Council, and the Swedish Foundation for Strategic Research. T.J.A. acknowledges partial support from the Polish National Science Center.

REFERENCES AND NOTES

1. Kittel, C. *Introduction to Solid State Physics*; John Wiley and Sons, 2005.
2. Shechtman, D.; Blech, I.; Gratias, D.; Cahn, J. W. Metallic Phase with Long-Range Orientational Order and No Translational Symmetry. *Phys. Rev. Lett.* **1984**, *53*, 1951–1953.
3. Levine, D.; Steinhardt, P. J. Quasicrystals: A New Class of Ordered Structures. *Phys. Rev. Lett.* **1984**, *53*, 2477–2480.
4. Janot, C. *Quasicrystals, a Primer*; Oxford University Press, 1997.
5. Trebin, H. R. *Quasicrystals. Structure and Physical Properties*; John Wiley and Sons, 2006.
6. Mahler, L.; Tredicucci, A.; Beltram, F.; Walther, C.; Faist, J.; Beere, H. E.; Ritchie, D. A.; Wiersma, D. S. Quasi-Periodic Distributed Feedback Laser. *Nat. Photonics* **2010**, *4*, 165–169.
7. Feng, Z.; Zhang, X.; Wang, Y.; Li, Z.-Y.; Cheng, B.; Zhang, D.-Z. Negative Refraction and Imaging Using 12-fold-Symmetry Quasicrystals. *Phys. Rev. Lett.* **2005**, *94*, 247402–247405.
8. Jin, C.; Cheng, B.; Man, B.; Li, Z.; Zhang, D.; Ban, S.; Sun, B. Band Gap and Wave Guiding Effect in a Quasiperiodic Photonic Crystal. *Appl. Phys. Lett.* **1999**, *75*, 1848–1850.
9. Lawrence, N.; Trevino, J.; Dal Negro, L. Aperiodic Arrays of Active Nanopillars for Radiation Engineering. *J. Appl. Phys.* **2012**, *111*, 113101.
10. Levi, L.; Rechtsman, M.; Freedman, B.; Schwartz, T.; Manela, O.; Segev, M. Disorder-Enhanced Transport in Photonic Quasicrystals. *Science* **2011**, *332*, 1541–1544.
11. Macia, E. Exploiting Aperiodic Designs in Nanophotonic Devices. *Rep. Prog. Phys.* **2012**, *75*, 036502.
12. Vardeny, Z. V.; Nahata, A.; Agrawal, A. Optics of Photonic Quasicrystals. *Nat. Photonics* **2013**, *7*, 177–187.
13. Zoorob, M. E.; Charlton, M. D. B.; Parker, G. J.; Baumberg, J. J.; Netti, M. C. Complete Photonic Bandgaps in 12-Fold Symmetric Quasicrystals. *Nature* **2000**, *404*, 740–743.
14. Wang, K. Structural Effects on Light Wave Behavior in Quasiperiodic Regular and Decagonal Penrose-Tiling Dielectric Media: A Comparative Study. *Phys. Rev. B* **2007**, *76*, 085107–085115.
15. Huang, F. M.; Zheludev, N.; Chen, Y.; Javier Garcia de Abajo, F. Focusing of Light by a Nanohole Array. *Appl. Phys. Lett.* **2007**, *90*, 091119–091121.
16. Gopinath, A.; Boriskina, S. V.; Feng, N.-N.; Reinhard, B. M.; Negro, L. D. Photonic-Plasmonic Scattering Resonances in Deterministic Aperiodic Structures. *Nano Lett.* **2008**, *8*, 2423–2431.
17. Deng, Z.-L.; Li, Z.-H.; Dong, J.-W.; Wang, H.-Z. In-Plane Plasmonic Modes in a Quasicrystalline Array of Metal Nanoparticles. *Plasmonics* **2011**, *6*, 507–514.
18. Bauer, C.; Kobiela, G.; Giessen, H. Optical Properties of Two-Dimensional Quasicrystalline Plasmonic Arrays. *Phys. Rev. B* **2011**, *84*, 193104–193114.
19. Bauer, C.; Kobiela, G.; Giessen, H. 2D Quasiperiodic Plasmonic Crystals. *Sci. Rep.* **2012**, *2*, 681.
20. Kruk, S. S.; Helgert, C.; Decker, M.; Staude, I.; Menzel, C.; Etrich, C.; Rockstuhl, C.; Jagadish, C.; Pertsch, T.; Neshev, D. N.; *et al*. Optical Metamaterials with Quasicrystalline Symmetry: Symmetry-Induced Optical Isotropy. *Phys. Rev. B* **2013**, *88*, 201404–20140.
21. Talapin, D. V.; Shevchenko, E. V.; Bodnarchuk, M. I.; Ye, X.; Chen, J.; Murray, C. B. Quasicrystalline Order in Self-Assembled Binary Nanoparticle Superlattices. *Nature* **2009**, 461–465.
22. Trevino, J.; Cao, H.; Dal Negro, L. Circularly Symmetric Light Scattering from Nanoplasmonic Spirals. *Nano Lett.* **2011**, *11*, 2008–2016.
23. Przybilla, F.; Genet, C.; Ebbesen, T. W. Enhanced Transmission through Penrose Subwavelength Hole Arrays. *Appl. Phys. Lett.* **2006**, *89*, 8514–8525.
24. Matsui, T.; Agrawal, A.; Nahata, A.; Vardeny, Z. V. Transmission Resonances through Aperiodic Arrays of Subwavelength Apertures. *Nature* **2007**, *446*, 517–521.
25. Pacifici, D.; Lezec, H. J.; Sweatlock, L. A.; Walters, R. J.; Atwater, H. A. Universal Optical Transmission Features in Periodic and Quasiperiodic Hole Arrays. *Opt. Express* **2008**, *16*, 9222–9238.
26. Xue, J.; Dong, B.-Q.; Wang, X.; Yang, R.; Xu, Z.-C.; Chen, Y.; Huq, E.; Zeng, W.; Qu, X.-P.; Liu, R. Surface Plasmon Enhanced Transmission through Gold Planar Crystals with Various Aperture Arrangements. *Microelectron. Eng.* **2010**, *87*, 1340–1343. The 35th International Conference on Micro- and Nano-Engineering (MNE).
27. Huang, F. M.; Zheludev, N.; Chen, Y.; Javier Garcia de Abajo, F. Focusing of Light by a Nanohole Array. *Appl. Phys. Lett.* **2007**, *90*, 091119.
28. Huang, F. M.; Chen, Y.; de Abajo, F. J. G.; Zheludev, N. I. Optical Super-Resolution through Super-Oscillations. *J. Opt. A: Pure Appl. Opt.* **2007**, *9*, S285–S293.
29. Huang, Y.-F.; Chattopadhyay, S.; Jen, Y.-J.; Peng, C.-Y.; Liu, T.-A.; Hsu, Y.-K.; Pan, C.-L.; Lo, H.-C.; Hsu, C.-H.; Chang, Y.-H.; *et al*. Improved Broadband and Quasi-Omnidirectional Anti-Reflection Properties with Biomimetic Silicon Nanostructures. *Nat. Nanotechnol.* **2007**, *2*, 770–774.
30. Bauer, C.; Giessen, H. Light Harvesting Enhancement in Solar Cells with Quasicrystalline Plasmonic Structures. *Opt. Express* **2013**, *21*, A363–A371.
31. Trevino, J.; Forestiere, C.; Martino, G. D.; Yerci, S.; Priolo, F.; Negro, L. D. Plasmonic-Photonic Arrays with Aperiodic Spiral Order for Ultra-Thin Film Solar Cells. *Opt. Express* **2012**, *20*, A418–A430.
32. Boriskina, S. V.; Lee, S. Y. K.; Amsden, J. J.; Omenetto, F. G.; Negro, L. D. Formation of Colorimetric Fingerprints on Nano-Patterned Deterministic Aperiodic Surfaces. *Opt. Express* **2010**, *18*, 14568–14576.

33. Lee, S. Y.; Amsden, J. J.; Boriskina, S. V.; Gopinath, A.; Mitropolous, A.; Kaplan, D. L.; Omenetto, F. G.; Negro, L. D. Spatial and Spectral Detection of Protein Monolayers with Deterministic Aperiodic Arrays of Metal Nanoparticles. *Proc. Natl. Acad. Sci.* **2010**, *107*, 12086–12090.
34. Gopinath, A.; Boriskina, S. V.; Premasiri, W. R.; Ziegler, L.; Reinhard, B. M.; Dal Negro, L. Plasmonic Nanogalaxies: Multiscale Aperiodic Arrays for Surface-Enhanced Raman Sensing. *Nano Lett.* **2009**, *9*, 3922–3929.
35. Lubin, S. M.; Zhou, W.; Hryn, A. J.; Huntington, M. D.; Odom, T. W. High-Rotational Symmetry Lattices Fabricated by Moire Nanolithography. *Nano Lett.* **2012**, *12*, 4948–4952.
36. Lubin, S. M.; Hryn, A. J.; Huntington, M. D.; Engel, C. J.; Odom, T. W. Quasiperiodic Moire Plasmonic Crystals. *ACS Nano* **2013**, *7*, 11035–11042.
37. Zhai, T.; Lin, Y.; Liu, H.; Zhang, X. Solution-Processable Complex Plasmonic Quasicrystals. *Opt. Express* **2013**, *21*, 28444–28449.
38. Socolar, J. E. S.; Steinhardt, P. J. Quasicrystals. II. Unit-Cell Configurations. *Phys. Rev. B* **1986**, *34*, 617–647.
39. Penrose, R. Pentaplexity A Class of Non-Periodic Tilings of the Plane. *Math. Intell.* **1979**, *2*, 32–37.
40. Hanarp, P.; Käll, M.; Sutherland, D. S. Optical Properties of Short Range Ordered Arrays of Nanometer Gold Disks Prepared by Colloidal Lithography. *J. Phys. Chem. B* **2003**, *107*, 5768–5772.
41. Haynes, C. L.; McFarland, A. D.; Zhao, L.; Van Duyne, R. P.; Schatz, G. C.; Gunnarsson, L.; Prikulis, J.; Kasemo, B.; Käll, M. Nanoparticle Optics. The Importance of Radiative Dipole Coupling in Two-Dimensional Nanoparticle Arrays. *J. Phys. Chem. B* **2003**, *107*, 7337–7342.
42. Gunnarsson, L.; Rindzevicius, T.; Prikulis, J.; Kasemo, B.; Käll, M.; Zou, S.; Schatz, G. C. Confined Plasmons in Nanofabricated Single Silver Particle Pairs: Experimental Observations of Strong Interparticle Interactions. *J. Phys. Chem. B* **2005**, *109*, 1079–1087.
43. Hicks, E. M.; Zou, S.; Schatz, G. C.; Spears, K. G.; Van Duyne, R. P.; Gunnarsson, L.; Rindzevicius, T.; Kasemo, B.; Käll, M. Controlling Plasmon Line Shapes through Diffractive Coupling in Linear Arrays of Cylindrical Nanoparticles Fabricated by Electron Beam Lithography. *Nano Lett.* **2005**, *5*, 1065–1070.
44. Hecht, E. *Optics*; Addison-Wesley Publishing Company, 2002.
45. Schwind, M.; Miljkovic, V. D.; Zäch, M.; Gusak, V.; Käll, M.; Zoric, I.; Johansson, P. Diffraction from Arrays of Plasmonic Nanoparticles with Short-Range Lateral Order. *ACS Nano* **2012**, *6*, 9455–9465.
46. Shegai, T.; Miljkovic, V. D.; Bao, K.; Xu, H.; Nordlander, P.; Johansson, P.; Käll, M. Unidirectional Broadband Light Emission from Supported Plasmonic Nanowires. *Nano Lett.* **2011**, *11*, 706–711.
47. Lieb, M. A.; Zavislan, J. M.; Novotny, L. Single-Molecule Orientations Determined by Direct Emission Pattern Imaging. *J. Opt. Soc. Am. B* **2004**, *21*, 1210–1215.
48. Antosiewicz, T.; Apell, S.; Zach, M.; Zoric, I.; Langhammer, C. Oscillatory Optical Response of an Amorphus Two Dimensional Array of Gold Nanoparticles. *Phys. Rev. Lett.* **2012**, *109*, 247401.
49. Johnson, P. B.; Christy, R. W. Optical Constants of the Noble Metals. *Phys. Rev. B* **1972**, *6*, 4370–4379.
50. Lodewijks, K.; Ryken, J.; Roy, W.; Borghs, G.; Lagae, L.; Dorpe, P. Tuning the Fano Resonance between Localized and Propagating Surface Plasmon Resonances for Refractive Index Sensing Applications. *Plasmonics* **2013**, *8*, 1379–1385.
51. Lozano, G. D.; Louwers, D. J.; Rodriguez, S. R. K.; Murai, S.; Jansen, O. T. A.; Verschuuren, M. A.; Rivas, J. G. Plasmonics for Solid-State Lighting: Enhanced Excitation and Directional Emission of Highly Efficient Light Sources. *Light: Sci. Appl.* **2013**, *2*, e66.
52. Kosako, T.; Kadoya, Y.; Hofmann, H. F. Directional Control of Light by a Nano-Optical Yagi-Uda Antenna. *Nat. Photonics* **2010**, *4*, 312–315.
53. Shegai, T.; Chen, S.; Miljkovic, V. D.; Zengin, G.; Johansson, P.; Käll, M. A Bimetallic Nanoantenna for Directional Colour Routing. *Nat. Commun.* **2011**, *2*, 481–486.
54. Schoen, D. T.; Coenen, T.; Garcia de Abajo, F. J.; Brongersma, M. L.; Polman, A. The Planar Parabolic Optical Antenna. *Nano Lett.* **2013**, *13*, 188–193.
55. Zhang, Y.; Barhoumi, A.; Lassiter, J. B.; Halas, N. J. Orientation-Preserving Transfer and Directional Light Scattering from Individual Light-Bending Nanoparticles. *Nano Lett.* **2011**, *11*, 1838–1844.
56. Taminiau, T. H.; Stefani, F. D.; B, S.; van Hulst, N. F. Optical Antennas Direct Single-Molecule Emission. *Nat. Photonics* **2008**, *2*, 234–237.
57. Taminiau, T. H.; Moerland, R. J.; Segerink, F. B.; Kuipers, L.; van Hulst, N. F. Resonance of an Optical Monopole Antenna Probed by Single Molecule Fluorescence. *Nano Lett.* **2007**, *7*, 28–33.
58. Urena, E. B.; Kreuzer, M. P.; Itzhakov, S.; Rigneault, H.; Quidant, R.; Oron, D.; Wenger, J. Excitation Enhancement of a Quantum Dot Coupled to a Plasmonic Antenna. *Adv. Mater.* **2012**, *24*, OP314–OP320.